Polarization-Dependent, Frequency-Selective THz Stereometamaterial Perfect Absorber

Mohammad Parvinnezhad Hokmabadi, David S. Wilbert, Patrick Kung, and Seongsin M. Kim*

Electrical and Computer Engineering Department, University of Alabama, Tuscaloosa, Alabama 35487, USA

(Received 27 December 2013; revised manuscript received 24 March 2014; published 15 May 2014)

We present design, fabrication, and characterization of THz stereometamaterial perfect absorber devices. Stereometamaterials consist of a three-dimensional lattice of meta-atoms, which exhibits distinct optical properties depending on the spatial arrangement of the meta-atoms in the unit cell. Integrated into a perfect absorber structure, the absorption and reflection properties of such devices at resonant frequencies reveal unique characteristics that are controlled by the polarization of the incident wave. Because of the break in reflection symmetry, such devices act as polarization-dependent passive switches, with the frequency response of a single band or a dual band absorber. The observed behavior is interpreted in terms of dipole-dipole interaction between the dipoles of the meta-atoms and their mirror images with respect to the metal backplane.

DOI: 10.1103/PhysRevApplied.1.044003

I. INTRODUCTION

Inspired by Veselago's theoretical predictions [1] and Pendry's pioneering experimental work [2,3], research in metamaterials is flourishing in the field of photonics. Metamaterials designed to render desired optical properties are realized by assembling subwavelength unit cells called meta-atoms [4–7], which are developed in various types such as spiral [8], fishnet [9], labyrinth [10], and electric field coupled [11] resonators, and can lead to various applications such as image compression [12], superlenses [13], cloaking [14], and optical black holes [15]. Among them, terahertz (THz) metamaterial perfect absorbers recently attracted a great amount of attention because of their potential application as sensors and detectors operating at THz frequencies [16]. Terahertz waves spanning from 0.1 to 10 THz are not fully utilized mainly due to the lack of high-performance sources, detectors, and availability of other optical components but are considered one of the most intriguing electromagnetic waves that can be used from fundamental physical sciences to biomedical imaging [17–23].

THz metamaterials perfect absorbers consist of a periodic frequency-selective surface (FSS), a dielectric spacer, and metal backplane. Since their first demonstration [16], these devices have been rapidly developed to exhibit multiple different functionalities such as polarization independence [24,25], multiband [26,27], and broadband response, which are desirable properties for many different sensors and detectors [28–30]. In addition, there is a strong driving force to study asymmetric metamaterials and their frequency response properties to achieve customized functionalities like negative refractive index in chiral materials [31–33] and circular polarization rotation in helical metamaterials [34–36]. The asymmetric properties of such metamaterials originate not only from the asymmetry within the individual meta-atoms but also from the asymmetric spatial arrangement of the meta-atoms with respect to one another and their collective interactions, similar to what is found in natural materials.

First introduced by Liu [37], stereometamaterials are composed of the same meta-atoms but artificially laid out with different spatial arrangements, similar to stereoisomers, which have the same chemical formula but different configurations of atoms within, resulting in distinct frequency response and unique properties. However, fundamental understanding is limited, with investigations limited to the transmission response of split ring resonators in which a break in symmetry is accomplished with different coupling angles of the resonator gaps.

In this work, we present a demonstration of a THz stereometamaterial perfect absorber device that reveals distinct absorption and reflection properties at resonant frequencies selected by the polarization of the incident wave. Our device is composed of two nonconcentric copper (Cu) rings tightly coupled to each other via a thin polyimide layer and act as the meta-atoms of the stereometamaterial FSS placed on a polyimide spacer layer and on a Cu backplane. Our hypothesis is that, when the stereometamaterial FSS is placed within subwavelength proximity of the conducting plane, one can expect to observe an asymmetric frequency response because of the break in the reflection symmetry that results from the meta-atoms interacting with their mirror images with respect to the metal plane. We demonstrate that our THz device has a rotationally asymmetric absorption behavior despite rotational symmetry of meta-atoms, such that it can work as a single band or a dual

*Author to whom correspondence should be addressed. seongsin@eng.ua.edu

 © 2014 American Physical Society

band absorber, as a polarization-dependent passive absorption switch, or a frequency-selective polarizing absorber. Furthermore, we gain fundamental understanding into this asymmetric frequency response by developing a physical interpretation based on the coupling of electric and magnetic dipoles on FSS and their mirror images with respect to the metal backplane.

II. DESIGN, FABRICATION, AND MEASUREMENT

Figure 1 illustrates the structure of the device studied here. Figures 1(a) and 1(b) show the three-dimensional schematics of a stereometamaterial absorber under 0° and 90° incident polarization, and Figs. 1(c) and 1(d) are front and side view illustrations of the device, respectively. We first use finite element method simulation to help design the device, including determining the expected electromagnetic response as a function of the device geometry or spatial arrangement by utilizing COSMOL MULTIPHYSICS. In simulation, we consider the periodic condition for side boundaries and the scattering condition for the front and back boundaries of the unit cell. A continuous plane wave source illuminates the unit cell at a normal incident angle. We use 327 710 triangular and tetrahedral mesh elements in each simulation. Since there is no transmission through the Cu backplane of the structure, we calculate the absorption by $A = 1 - R$, where A is the absorption, and R is the reflection from the structure. We use Cu conductivity of 6×10^7 S/m and polyimide conductivity and permittivity of 6.67×10^{-16} S/m and $3.15 + j0.1$, respectively. Two individual ring-polyimide-backplane absorbers are first designed to exhibit near perfect absorption at 0.750 and 0.810 THz by slightly modifying the ring dimensions. The simulation yields values of 39 and 42 μm for the inner ($R1_{in}$) and outer ($R1_{out}$) radii, respectively, where an 11.55-μm polyimide total thickness (Sep + Lon + t) is obtained for the absorber with the resonance at 0.750 THz. To exhibit perfect absorption at 0.810 THz, the inner ($R2_{in}$) and outer ($R2_{out}$) radii for the other single ring absorber are found to be 33 and 36 μm, respectively, with a 9.6-μm-thick polyimide spacer (Sep). The Cu thickness (t) is maintained at 200 nm in all simulations.

The fundamental design of our stereometamaterial absorber consists of combining these two single ring absorbers in the manner shown in Fig. 1, where Lon and Lat are the center-to-center distances between two rings in the z (longitudinal) and y (lateral) directions, respectively. In the first iteration of this design, Lon is set equal to 1.75 μm. However, to gain better understanding of the impact of various spatial arrangement configurations on the stereometamaterial absorption behavior, Lat is swept from 0 up to 16 μm under different incident field polarization

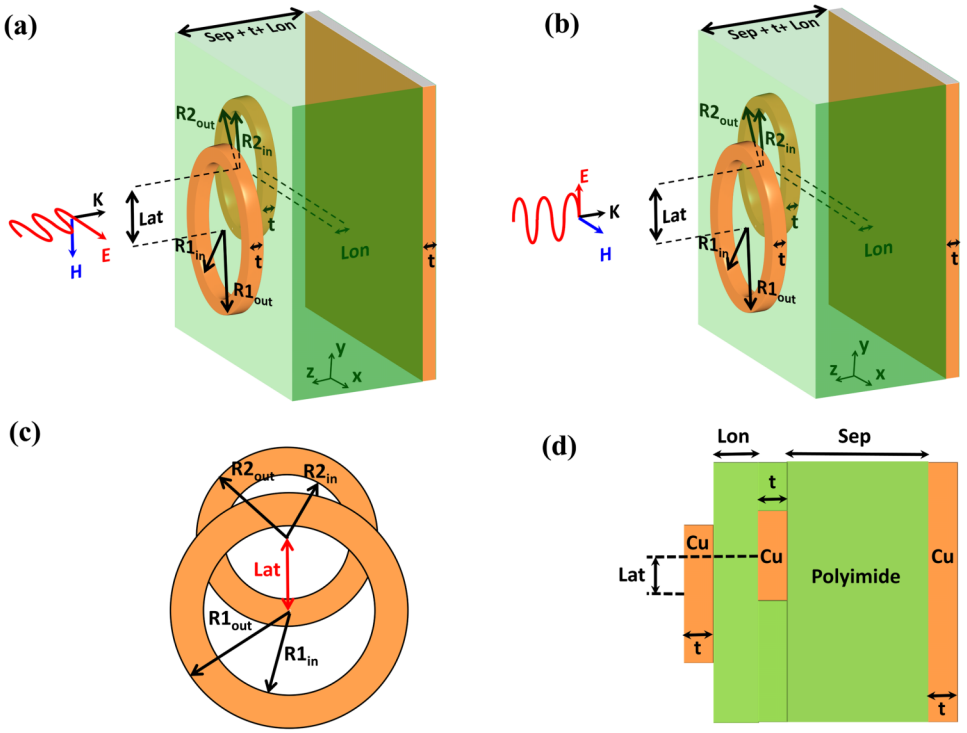

FIG. 1. Schematic illustration of the stereometamaterial absorber. (a) and (b) illustrate three-dimensional schematics of the stereometamaterial absorber under 0° and 90° incident polarization, respectively. (c) Front view illustration of the FSS and (d) side view illustration of the stereometamaterial absorber. $R1_{in}$, $R1_{out}$, $R2_{in}$, $R2_{out}$ are inner and outer radii of front and back rings, respectively, t is the thickness of rings and Cu backplane, and Lon and Lat are the center-to-center distances between rings in z and y directions, respectively.

TABLE I. Dimensions (μm) associated with the stereometamaterial absorber.

$R1_{in}$	$R1_{out}$	$R2_{in}$	$R2_{out}$	Lon	t	Sep	d	Lat[a]
39	42	33	36	1.75	0.2	9.6	104	0–16

[a]After sweeping Lat, the value 12 μm is chosen to illustrate the discussion in this paper.

angles. The dimensions of the structure and simulation conditions are summarized in Table I.

Changing Lat together with the incident polarization angle alters the symmetry of the structure, which leads to unique near field coupling schemes among the meta-atoms (rings) and their images on the backplane and, thus, extraordinary absorption spectra of the stereometamaterial absorber when in different configurations. Figure 2 shows the strength of the absorption as a function of frequency and Lat for 0° and 90° incident polarization angles. When Lat is zero, the absorber is symmetric with respect to the polarization angle, and, therefore, the response will be identical for all polarizations. Similar cases are reported in detail [38]. However, increasing Lat leads to a very different behavior of the absorption spectra for the 0° and 90° polarizations. By increasing Lat from 0 to 8 μm by contrast to the 0° configuration, a second strong absorption peak appears in the 90° polarization case, which results in a broadband absorption. Above 8 μm, the frequency response of the absorber changes for both polarizations but in the opposite manner: the resonance blueshifts in the 0° case while it redshifts in the 90° configuration. This characteristic makes such a structure applicable as a polarization-dependent stereometamaterial reflection or absorption switch when Lat is between 10 and 16 μm. For the rest of the discussion, Lat is fixed equal to 12 μm, which is depicted with a white line in Fig. 2. In this case, the device switches its resonance between 0.725 and 0.790 THz by rotating around the z axis.

Fabrication of the designed device is done by using standard lift-off photolithography. The Cu backplane and rings are deposited by electron beam evaporation with the rings patterned by standard photolithography. The polyimide spacer layer and the polyimide layer between the rings are deposited by spin coating to achieve the desired thicknesses. The polyimide is baked in nitrogen at 350 °C for an hour to ensure complete curing. For measurement, the reflectivity of the arrays is measured by reflection mode THz time-domain spectroscopy under clean dry air purge at normal incidence. Broadband THz radiation (0.3 to 3.0 THz) is generated by a high voltage biased photoconductive antenna pumped by a 775-nm ultrafast Ti:sapphire laser with 76-MHz repetition rate. An electro-optic sampling scheme is used for time-domain signal detection using ZnTe crystal. An optical delay line is utilized to vary the timing of the detection pulse. In order to measure the sample response under different polarization angles, the sample is rotated with respect to the normal axis [39,40].

III. RESULTS AND DISCUSSION

Figures 3(a) and 3(b) show the simulated and measured absorption spectra of the device for various polarization angles. As shown, the resonance frequency switches from 0.725 to 0.790 THz gradually when the polarization angle decreases from 90° to 0°, which is indicated by two vertical arrows in Fig. 3(a). Figure 3(c) shows that the experimental and simulation absorption results are in good agreement. At 45°, however, the two separate resonances are not well resolved compared to the simulation results. This is mainly due to the limitation of the system resolution, which is coarser than 50 GHz and the effect of a fast Fourier transform. In addition, it might originate from a broadening of absorption spectra in experiment compared to simulation due to slightly different Cu conductivity and polyimide loss of a fabricated sample that is not considered in simulation. The effect of this broadening becomes much more clearly observable when there exist two excited resonances close to each other as shown in 45° polarization, such that the sidebands of two excited resonances overlap each other and

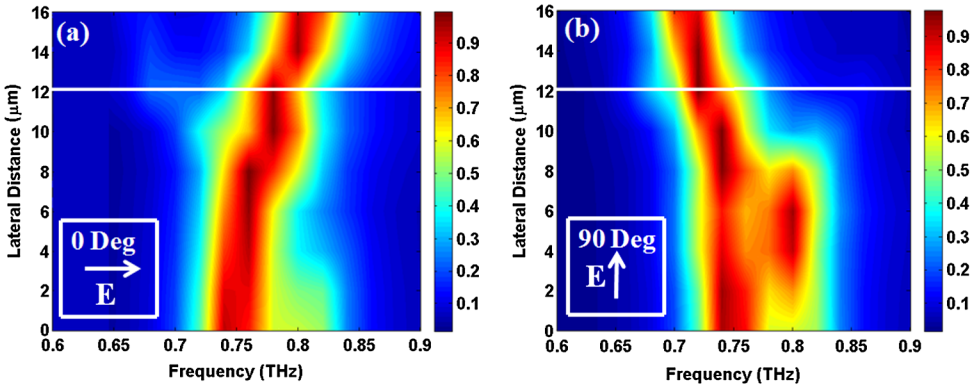

FIG. 2. Absorption spectrum versus frequency and lateral distance (Lat) between rings. (a) 0° and (b) 90° incident polarizations. White lines indicate the Lat chosen for the switch discussed in the rest of in this paper.

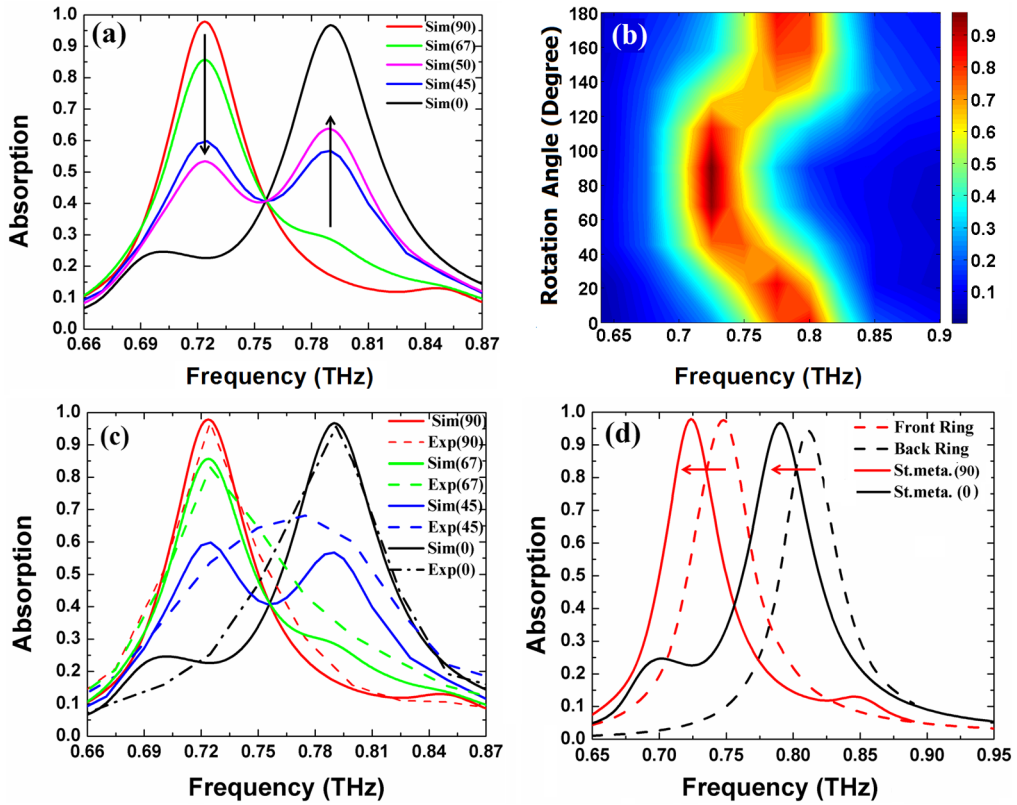

FIG. 3. Comparison between simulation and experiment results. (a) Simulated absorption spectra for different polarizations (red 90°, green 67°, pink 50°, blue 45°, and black 0°), (b) experimentally measured absorption versus frequency and rotation angle of the sample, (c) comparison between measurement (dashed lines) and simulation (solid lines) results for different polarization angles, and (d) comparison of the absorption spectra between single ring absorbers (dashed curves) and stereometamaterial absorber in 0° and 90° polarizations (solid curves).

eliminate the contrast between them. Figure 3(d) compares the simulated spectra of the single ring absorbers and those of the stereometamaterial absorber at 0° and 90° polarization angles showing that the resonances of the stereometamaterial absorber at 0° and 90° are associated with the back and front rings, respectively, and are also both redshifted from the resonances of individual rings.

To better understand what the physical origins of these observed phenomena are and the function of the stereometamaterial absorber device, we analyze the electric fields and current densities at various polarization angles. Figures 4(a)–4(f) show the electric field and current density (x component) distributions on the front ring, back ring, and metal backplane at 0.725 THz corresponding to the resonance at 90° polarization. Black arrows have been added in the current density (J) illustrations [Figs. 4(b)–4(f)] to show the direction of each current for clarity. The emergence of an electric dipole on the front ring [Fig. 4(a)] indicates that this resonance originates from the front ring. The corresponding current associated with this dipole [Fig. 4(b)] is in the opposite direction to that in the backplane [Fig. 4(f)].

In addition to the front ring dipole, another dipole is observed on the back ring in which the upper pole is

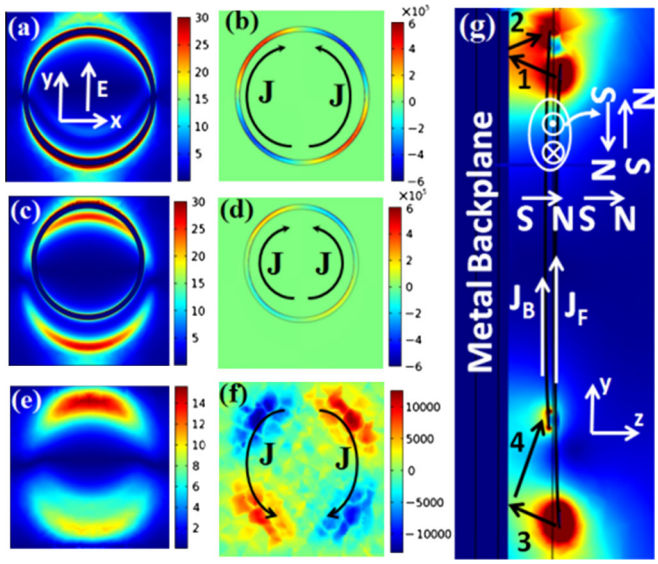

FIG. 4. Electric field and current density distributions in 90° polarization at 0.725 THz. Electric field and current density (x component) distributions on front ring [(a),(b)], back ring [(c),(d)], and metal backplane [(e),(f)] in 90° polarization at 0.725 THz. (g) A side view of the electric field profile in the stereometamaterial absorber in 90° polarization at 0.725 THz.

stronger than the pole in the down side [Fig. 4(c)]. We call the dipole on the front ring the FR dipole and the one on the back ring the BR dipole for clarity. Figure 4(g) is a side view of the electric fields in the structure and clearly shows the two poles of the BR dipole indicated by the black arrows 2 and 4. The origin of the BR dipole, which generates a current [Fig. 4(d)] parallel to that of the front ring, is more subtle. Since the electric dipole moments on both rings are oriented in the same direction, the creation of the BR dipole is not due to direct induction from the front ring. Furthermore, the BR dipole is still observed in simulations with a larger lattice constant ($d = 150\ \mu$m), i.e., the unit cell, implying that this dipole does not originate from the interaction between rings in adjacent unit cells either. This is in stark contrast with our previous observation of antiparallel dipole moments when two rings are concentric (Lat = 0) [38]. We, therefore, believe that the BR dipole arises from the induction effects of currents in the backplane. As illustrated schematically in Fig. 4(g), the upper pole of the front ring induces opposite charges (image pole) on the backplane (indicated with arrow 1), which then induces the upper pole on the back ring (indicated with arrow 2). By contrast, although the lower pole of the front ring induces an image pole on the backplane (indicated with arrow 3), the lower semicircle of the back ring is farther from that image pole because of the rotational asymmetry of the back ring with respect to the center of the unit cell. Therefore, the bottom pole is less strong than the upper one in the back ring (indicated with arrow 4).

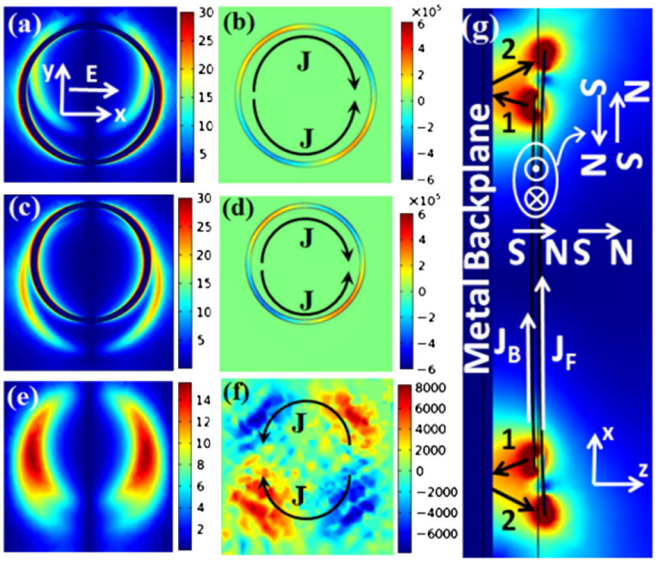

FIG. 5. Electric field and current density distributions in 0° polarization at 0.790 THz. Electric field and y component of the current density on the front ring [(a),(b)], back ring [(c),(d)], and metal backplane [(e),(f)] in 0° polarization at 0.790 THz. (g) The top view of the electric field profile in stereometamaterial absorber in 0° polarization and at 0.790 THz.

Under the 0° incident polarization configuration, when the resonance frequency switched to 0.790 THz, the electric field and current density distributions are shown in Figs. 5(a)–5(g), in which the y components of the electric currents are illustrated. Since this resonance occurs at a higher frequency than for the 90° polarization, it should arise from the smaller (i.e., back) ring. However, in addition to the electric dipole on the back ring [Fig. 5(c)], another dipole is also observed on the front ring with comparable electric field intensity [Fig. 5(a)]. This dipole comes from the induction effect of the metal backplane: the poles on the back ring induce image poles on the metal backplane [indicated with arrow 1 in Fig. 5(g)], which, in turn, induce the poles on the front ring [indicated with arrow 2 in Fig. 5(g)]. However, unlike the 90° polarization, both poles have identically strong intensities in this case, because both semicircles of the front ring have identical distance from the corresponding image poles.

The absorption process can be explained on the basis of the excited effective electric dipole associated with the stereometamaterial FSS and its image dipole ("imaged" with respect to the metal backplane), as illustrated in Fig. 6(a). The excited dipole (P_{FSS}) irradiates a reflected wave (R_{FSS}). The image dipole (P_{image}) irradiates an electromagnetic wave that undergoes multiple reflections inside the cavity formed by the stereometamaterial FSS and backplane. If the thickness and refractive index of the spacer are chosen properly, then the resulting compounded wave (R_{im}) from the image dipole can be made exactly out of phase with that of the excited dipole (R_{FSS}), thus, resulting in a zero reflection (100% absorption) at the resonance frequency.

While the interaction between the FSS electric dipole and its image dipole leads to a zero reflection, the coupling between the magnetic fields of the rings lead to a redshift of the resonance frequency compared to those of the corresponding single ring absorbers. Although the net magnetic

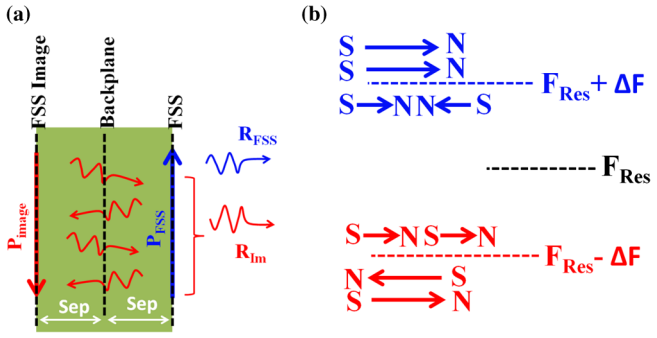

FIG. 6. Schematic of absorption process and magnetic dipoles interactions. (a) A schematic cross-section illustration of interaction between the electric dipoles on FSS and the metal backplane leading to the absorption process, and (b) the frequency level scheme of the coupling between magnetic dipoles resulting in the resonance frequency shift.

moments around the centers of the rings are close to zero due to the currents oscillating in opposite directions in the left and right semicircles of the rings, there are strong magnetic fields in close proximity to the rings. These magnetic fields will couple to each other in regions where the front and back rings are very close. This coupling is illustrated in Figs. 4(g) and 5(g): the parallel currents in the rings shown as J_F and J_B in the figures lead to centrifugal ($\times$) and centripetal ($\cdot$) magnetic fields in the region between the two rings (shown also as S $\rightarrow$ N and N $\rightarrow$ S) as well as magnetic fields parallel to the z axis that couple to one another to lower the resonance frequency. Figure 6(b) shows how these magnetic couplings lead to resonance frequency redshift by using the frequency level scheme of two coupled magnetic dipoles [37,41]. While the similar poles of magnetic dipoles repel each other, hence, increasing the restoring force and leading to frequency blueshift, the opposite poles of them attract each other, reducing the restoring force, and, hence, leading to frequency redshift, which is the case of magnetic fields coupling in our device.

The most interesting phenomenon occurs when the incident polarization angle is 45°. Figures 7(a) and 7(c) show the electric field profiles on the front ring and back ring at 0.725 THz, respectively, while Figs. 7(b) and 7(d) illustrate the same profiles at 0.790 THz. The reflected electric fields at 50 μm away from the absorber device are shown in Figs. 7(f) and 7(g) at their corresponding resonance frequencies. Although the incident electric field (white arrow E) is at a 45° angle, the dipole moments depicted by P1 and P2 associated, respectively, with the 0.725- and 0.790-THz resonances are nearly vertical and horizontal. Correspondingly, irradiated reflected waves out of those moments [Figs. 7(f) and 7(g)] possess almost vertical and horizontal polarizations.

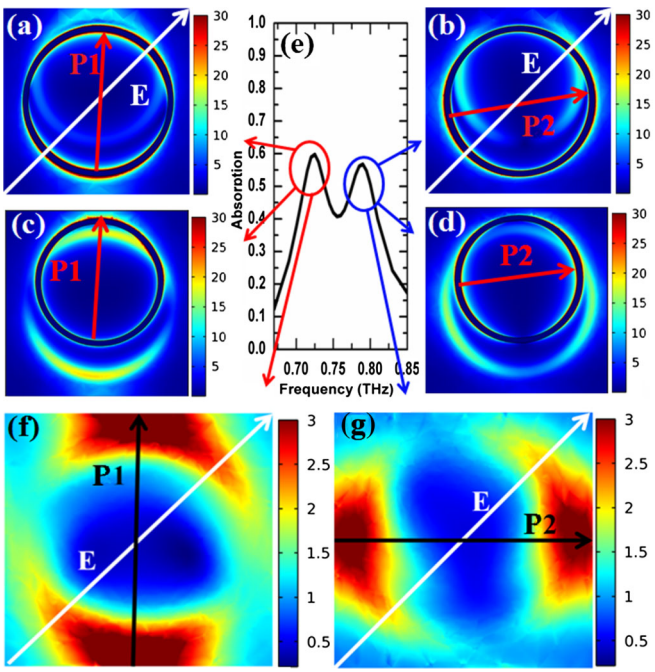

FIG. 7. Near field and far field electric field distribution at 45° polarization. Electric field on front ring [(a),(b)] and back ring [(c),(d)] in 45° polarization at 0.725 and 0.790 THz, respectively, with corresponding absorption spectrum (e). (f) and (g) are the reflected electric fields in 50 μm away (far field) from the absorber at indicated resonance frequency, respectively.

The response observed at 45° polarization can give us a glimpse of the chiral nature of the structure under that polarization. Indeed, at first glance, when considering only its own geometry, our structure seems to be achiral. However, when the polarization of the incident THz wave is taken into account, along with the resulting steady-state distribution of charges on the FSS rings and their images due to the metal backplane, the structure can exhibit chirality depending on the wave polarization angle. At 0° and 90° incident polarization, the distribution of charges (i.e., the appeared dipoles) in the structure can be superimposed with its mirror image by applying a translational followed by a rotational symmetry operation while in the 45° case no combination of such operations would bring about a superimposition of the resulted charge distribution and its mirror image. Consequently, according to the mathematical definition of chirality [42], the structure can exhibit polarization-dependent chirality. Further and thorough study of the polarization-dependent chirality of these structures will be necessary in the future.

IV. CONCLUSION

In summary, we study the characteristics of a stereometamaterial THz absorber based on two tightly coupled Cu rings and interpret the results using dipole-dipole interaction phenomena. Depending on the relative positions of the rings with respect to the incident wave polarization, the absorber exhibits multifunctional application such as dual band, single band, and broadband absorption, which is useful in dynamically tuning the response of the absorber. Accordingly, we design, fabricate, and measure such a polarization-dependent THz stereometamaterial device that switches a narrow absorption band from 0.725 to 0.790 THz by rotating the device relative to the polarization direction from 90° to 0°. The device also presents a polarizing effect at 45° incident polarization in the reflection mode.

ACKNOWLEDGMENTS

We would like to acknowledge NSF BRIGE (ECCS-0824452) and NSF CAREER for supporting this work.

[1] V. G. Veselago, The electrodynamics of substances with simultaneously negative values of $\mathcal{E}$ and μ, Sov. Phys. Usp. **10**, 509 (1968).

[2] J. B. Pendry, A. J. Holden, D. J. Robbins, and W. J. Stewart, Magnetism from conductors and enhanced nonlinear

phenomena, IEEE Trans. Microwave Theory Tech. **47**, 2075 (1999).
[3] J. B. Pendry, A. J. Holden, W. J. Stewart, and I. Youngs, Extremely low frequency plasmons in metallic mesostructures, Phys. Rev. Lett. **76**, 4773 (1996).
[4] A. Artar, A. A. Yanik, and H. Altug, Multispectral plasmon induced transparency in coupled meta-atoms, Nano Lett. **11**, 1685 (2011).
[5] V. M. Shalaev, Optical negative-index metamaterials, Nat. Photonics **1**, 41 (2007).
[6] C. Menzel, C. Helgert, C. Rockstuhl, E. B. Kley, A. Tunnermann, T. Pertsch, and F. Lederer, Asymmetric transmission of linearly polarized light at optical metamaterials, Phys. Rev. Lett. **104**, 253902 (2010).
[7] V. G. Veselago and E. E. Narimanov, The left hand of brightness: Past, present and future of negative index materials, Nat. Mater. **5**, 759 (2006).
[8] J. D. Baena, R. Marques, F. Medina, and J. Martel, Artificial magnetic metamaterial design by using spiral resonators, Phys. Rev. B **69**, 014402 (2004).
[9] J. Valentine, S. Zhang, T. Zentgraf, E. U. Avila, D. A. Genov, G. Bartal, and X. Zhang, Three-dimensional optical metamaterial with a negative refractive index, Nature (London) **455**, 376 (2008).
[10] I. Bulu, H. Caglayan, and E. Ozbay, Experimental demonstration of labyrinth-based left-handed metamaterials, Opt. Express **13**, 10238 (2005).
[11] D. Schurig, J. J. Mock, and D. R. Smith, Electric-field-coupled resonators for negative permittivity metamaterials, Appl. Phys. Lett. **88**, 041109 (2006).
[12] J. Hunt, T. Driscoll, A. Mrozack, G. Lipworth, M. Reynolds, D. Brady, and D. R. Smith, Metamaterial apertures for computational imaging, Science **339**, 310 (2013).
[13] X. Zhang and Z. Liu, Superlenses to overcome the diffraction limit, Nat. Mater. **7**, 435 (2008).
[14] N. Landy and D. R. Smith, A full-parameter unidirectional metamaterial cloak for microwaves, Nat. Mater. **12**, 25 (2013).
[15] E. E. Narimanov and A. V. Kildishev, Optical black hole: Broadband omnidirectional light absorber, Appl. Phys. Lett. **95**, 041106 (2009).
[16] H. Tao, N. I. Landy, C. M. Bingham, X. Zhang, R. D. Averitt, and W. J. Padilla, A metamaterial absorber for the terahertz regime: Design, fabrication and characterization, Opt. Express **16**, 7181 (2008).
[17] A. Markelz, S. Whitmire, J. Hillebrecht, and R. Birge, THz time domain spectroscopy of bimolecular conformational modes, Phys. Med. Biol. **47**, 3797 (2002).
[18] S. E. Whitmire, D. Wolpert, A. G. Markelz, J. R. Hillebrecht, J. Galan, and R. R. Birge, Protein flexibility and conformational state: A comparison of collective vibrational modes of wild-type and D96N bacteriorhodopsin, Biophys. J. **85**, 1269 (2003).
[19] M. Nagel, P. H. Bolivar, M. Brucherseifer, H. Kurz, A. Bosserhoff, and R. Buttner, Integrated THz technology for label-free genetic diagnostics, Appl. Phys. Lett. **80**, 154 (2002).
[20] R. M. Woodward, B. E. Cole, V. P. Wallace, R. J. Pye, D. D. Arnone, E. H. Linfield, and M. Pepper, Terahertz pulse imaging in reflection geometry of human skin cancer and skin tissue, Phys. Med. Biol. **47**, 3853 (2002).
[21] J. W. Waters *et al.*, The Earth observing system microwave limb sounder (EOS MLS) on the Aura satellite, IEEE Trans. Geosci. Remote Sens. **44**, 1075 (2006).
[22] R. Appleby, Standoff detection of weapons and contraband in the 100 GHz to 1 THz region, IEEE Trans. Antennas Propag. **55**, 2944 (2007).
[23] S. Balci, W. Baughman, D. S. Wilbert, G. Shen, P. Kung, and S. M. Kim, Characteristics of THz carrier dynamics in GaN thin film and ZnO nanowires by temperature dependent terahertz time domain spectroscopy measurement, Solid State Electron. **78**, 68 (2012).
[24] Y. Ma, Q. Chen, J. Grant, S. C. Saha, A. Khalid, and D. R. S. Cumming, A terahertz polarization insensitive dual band metamaterial absorber, Opt. Lett. **36**, 945 (2011).
[25] X. Shen, T. J. Cui, J. Zhao, H. F. Ma, W. X. Jiang, and H. Li, Polarization-independent wide-angle triple-band metamaterial absorber, Opt. Express **19**, 9401 (2011).
[26] X. Y. Peng, B. Wang, S. Lai, D. H. Zhang, and J. H. Teng, Ultrathin multi-band planar metamaterial absorber based on standing wave resonances, Opt. Express **20**, 27756 (2012).
[27] G. Dayal and S. A. Ramakrishna, Design of multi-band metamaterial perfect absorbers with stacked metal-dielectric disks J. Opt. **15**, 055106 (2013).
[28] L. Huang, D. R. Chowdhury, S. Ramani, M. T. Reiten, S. N. Luo, A. J. Taylor, and H. T. Chen, Experimental demonstration of terahertz metamaterial absorbers with a broad and flat high absorption band, Opt. Lett. **37**, 154 (2012).
[29] J. Sun, L. Liu, G. Dong, and J. Zhou, An extremely broad band metamaterial absorber based on destructive interference, Opt. Express **19**, 21155 (2011).
[30] C. M. Watts, X. Liu, and W. J. Padilla, Metamaterial electromagnetic wave absorbers, Adv. Mater. **24**, OP98 (2012).
[31] S. Zhang, Y. S. Park, J. Li, X. Lu, W. Zhang, and X. Zhang, Negative refractive index in chiral metamaterials, Phys. Rev. Lett. **102**, 023901 (2009).
[32] E. Plum, J. Zhou, J. Dong, V. A. Fedotov, T. Koschny, C. M. Soukoulis, and N. I. Zheludev, Metamaterials with negative index due to chirality, Phys. Rev. B **79**, 035407 (2009).
[33] B. Wang, J. Zhou, T. Koschny, and C. M. Souloulis, Nonplanar chiral metamaterials with negative index, Appl. Phys. Lett. **94**, 151112 (2009).
[34] B. Wang, J. Zhou, T. Koschny, M. Kafesaki, and C. M. Soukoulis, Chiral metamaterials: Simulations and experiments, J. Opt. A **11**, 114003 (2009).
[35] C. Rockstuhl, C. Menzel, T. Paul, and F. Lederer, Optical activity in chiral media composed of three-dimensional metallic meta-atoms, Phys. Rev. B **79**, 035321 (2009).
[36] J. K. Gansel, M. Thiel, M. S. Rill, M. Decker, K. Bade, V. Saile, G. V. Freymann, S. Linden, and M. Wegener, Gold helix photonic metamaterial as broadband circular polarizer, Science **325**, 1513 (2009).
[37] N. Liu, H. Liu, S. Zhu, and H. Giessen, Stereometamaterials, Nat. Photonics **3**, 157 (2009).
[38] M. P. Hokmabadi, D. S. Wilbert, P. Kung, and S. M. Kim, Theoretical and experimental investigation of hybrid broadband terahertz metamaterial absorber, Proc. SPIE Int. Soc. Opt. Eng. **8632**, 86321X (2013).

[39] D. S. Wilbert, M. P. Hokmabadi, P. Kung, and S. M. Kim, Equivalent-circuit interpretation of the polarization insensitive performance of the THz metamaterial absorbers, IEEE Trans. Terahertz Sci. Technol. **3**, 846 (2013).

[40] M. P. Hokmabadi, D. S. Wilbert, P. Kung, and S. M. Kim, Design and analysis of perfect terahertz metamaterial absorber by a novel dynamic circuit model, Opt. Express **21**, 16455 (2013).

[41] N. Liu and H. Giessen, Coupling effects in optical metamaterials, Angew. Chem., Int. Ed. **49**, 9838 (2010).

[42] M. Petitjean, Chirality in metric spaces, Symmetry **21**, 27 (2010).